Nanjo *et al. Earth, Planets and Space (2024) 76:55*
https://doi.org/10.1186/s40623-024-01995-9

Earth, Planets and Space

FULL PAPER **Open Access**

Post-midnight purple arc and patches appeared on the high latitude part of the auroral oval: Dawnside counterpart of STEVE?

Sota Nanjo[1,4*], Gabriel Arne Hofstra[2], Kazuo Shiokawa[3], Atsuki Shinbori[3], Satonori Nozawa[3] and Keisuke Hosokawa[1]

Abstract

The phenomenon known as strong thermal emission velocity enhancement (STEVE) is a purple/mauve arc-shaped atmospheric glow observed at lower latitudes of the auroral oval on the duskside. Simultaneous observations using a ground-based camera and a low-altitude satellite have shown that STEVE is accompanied by rapid westward ion flows. Such fast ion flows are termed the subauroral ion drift (SAID) or subauroral polarization stream (SAPS). Similarly, an eastward fast ion flow known as the dawnside auroral polarization stream (DAPS) is observed within the Region 1 current on the dawnside. If the optical phenomenon triggered by SAID/SAPS corresponds to STEVE, a comparable optical phenomenon should be driven by DAPS. Thus far, however, such a phenomenon has not been reported. This study discovers, for the first time, a purple-colored optical phenomenon characterized by the fast eastward ion flows, a possible signature of DAPS, occurring poleward of the bright green arc in the post-midnight sector. We present color all-sky images obtained by a ground-based commercial digital camera, along with wide-coverage optical measurements and in-situ data from low-altitude satellites. The results imply that this glow requires not only a high-speed ion flow but also its sharp latitudinal gradient at the boundary between the Region 1 and 2.

Keywords STEVE, DAPS, Commercial digital camera, Optical observation, Swarm, NOAA VIIRS, OMTI

---

*Correspondence:
Sota Nanjo
sota.nanjo@uec.ac.jp
Full list of author information is available at the end of the article

© The Author(s) 2024. **Open Access** This article is licensed under a Creative Commons Attribution 4.0 International License, which permits use, sharing, adaptation, distribution and reproduction in any medium or format, as long as you give appropriate credit to the original author(s) and the source, provide a link to the Creative Commons licence, and indicate if changes were made. The images or other third party material in this article are included in the article's Creative Commons licence, unless indicated otherwise in a credit line to the material. If material is not included in the article's Creative Commons licence and your intended use is not permitted by statutory regulation or exceeds the permitted use, you will need to obtain permission directly from the copyright holder. To view a copy of this licence, visit http://creativecommons.org/licenses/by/4.0/.

Graphical Abstract

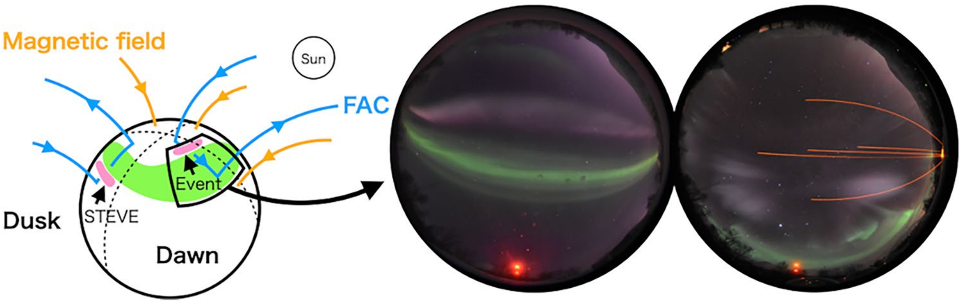

Introduction

Strong thermal emission velocity enhancement (STEVE) is an arc-shaped atmospheric optical phenomenon that exhibits purple/mauve hues (MacDonald et al. 2018). The glow occurs at altitudes ranging from 130 to 270 km (Archer et al. 2019), and sometimes, STEVE is observed alongside the green (557.7 nm) picket fence structure on its lower altitude part (Yadav et al. 2021; Martinis et al. 2022). The color of STEVE is a result of its continuous spectrum ranging from 400 to 700 nm, as revealed by the spectroscopic observation (Gillies et al. 2019). While the shape of STEVE is similar to that of a typical green auroral arc observed in the auroral latitudes, auroras have a discrete spectrum and are generated by the precipitation of electrons and protons from the magnetosphere. Considering this remarkable difference, STEVE is not an aurora. Both indeed have similar shapes but are distinctively different in color. As a result, distinguishing them in color images is easy but becomes challenging in black-and-white images that are frequently used for scientific research.

To clarify the generation mechanism of STEVE, a statistical analysis of the characteristics of STEVE, such as dependence on the geomagnetic activity and morphology, has been conducted (Gallardo-Lacourt et al. 2018). They identified 28 STEVE events with the time history of events and macroscale interactions during substorms (THEMIS) all-sky imagers, which measure emissions in visible bands panchromatically, and the redline emission geospace observatory, which is an all-sky camera (ASC) measuring the 630.0-nm oxygen emission. Their results indicate that STEVE is frequently observed 1 h after the onset of substorms in equinoxes and that the average geomagnetic conditions during STEVE are -20 nT for the Dst index and -400 nT for the AL index. Morphologically, the appearance of STEVE continues for 1 h, exhibiting narrow ($\sim$20 km) latitudinal and broad (>2000 km) longitudinal structures. Interestingly, it has shown that STEVE does not necessarily require a highly disturbed condition (Nishimura et al. 2023b, and references therein).

MacDonald et al. (2018) found a fast ($\sim$5.5 km/s) westward ion flow, depletion in the electron density, and enhancement of the electron temperature within STEVE by analyzing a simultaneous observation event with optical observations by ground-based cameras and in-situ measurements by a low-Earth orbiting (LEO) satellite. These characteristics are similar to those of the subauroral ion drift (SAID) (Anderson et al. 1993, 2001). SAID is a transient phenomenon that occurs in the sub-auroral region in the pre-midnight sector, which is similar to the occurrence characteristics of STEVE. Considering these similarities between STEVE and SAID and the continuous spectrum of STEVE, some researchers have suggested a hypothesis that STEVE's emission might be generated through atmospheric heating induced by the rapid westward ion drift (Gillies et al. 2019; Mende et al. 2019; Harding et al. 2020; Mishin and Streltsov 2022).

SAIDs are known to occur with Region 2 (R2) field-aligned currents (FACs) that are downward on the duskside (Zmuda and Armstrong 1974; Iijima and Potemra 1976). This area has low conductivity due to the lack of particle precipitation. The downward FACs are connected to the upward FACs via Pedersen currents, resulting in the generation of a strong northward (poleward) electric field within this low-conductivity region. Galperin et al. (1973) verified the existence of such a strong electric field using the observation from an LEO satellite. This electric field excites the localized westward plasma flow ($\mathbf{E} \times \mathbf{B}$ drift), and it is termed Polarization Jet (Galperin et al. 1973), SAID (Spiro et al. 1979), or Sub-Auroral Electric Field (Karlsson et al. 1998). Later, satellite and radar observations have revealed that the westward flow sometimes has a wide latitudinal distribution in the sub-auroral region, and Foster and Vo (2002) named this flow Sub-Auroral Polarization Stream (SAPS).

STEVE is observed in the pre-midnight sector. SAID/SAPS are also duskside phenomena, but a similar flow called Dawnside Auroral Polarization Stream (DAPS) was identified on the dawnside in the Rice-Convection-Model simulation and the observation of LEO satellites (Gkioulidou et al. 2009; Liu et al. 2020). DAPS is triggered in the return flow region of the dawnside convection cell and characterized by a fast eastward flow exceeding 1 km/s within Region 1 (R1) FAC. Analogous to SAPS, DAPS occurs within the downward FAC region, but while SAPS is a subauroral phenomenon on the duskside, DAPS occurs in the high latitude part of the auroral oval on the dawnside. In this region, the electric field intensified by the latitudinal gradient of the conductivity is equatorward, the corresponding plasma flow being eastward. DAPS is also a fast plasma flow; hence, if STEVE's emission is generated by fast plasma flows, we should observe a comparable glow even in the post-midnight sector with eastward fast flows. Thus far, however, no such phenomenon has been reported.

Another interesting aspect of STEVE is its engagement with citizen science. Commercial digital camera observations by photographers have contributed to unveiling the nature of STEVE, particularly concerning its color (e.g., Semeter et al. 2020; Chu et al. 2020; Martinis et al. 2022). Digital cameras are not often used in scientific optical observations because the transmission characteristics of the color filter are unknown, and it is difficult to convert the raw count in the image into physical quantities. On the other hand, the use of color images from digital cameras makes it easy to distinguish STEVE and a normal green auroral arc, both of which have a similar arc-like shape.

Nanjo et al. (2022) has developed Tromsø AI (https://tromsoe-ai.cei.uec.ac.jp), a web application that provides real-time notification of the auroral appearance in Tromsø and Skibotn in Norway and Kiruna in Sweden, for both of applied optical observations and encouragement of citizen science. A photographer utilizing Tromsø AI for his work found peculiar optical phenomena that showed a similar color to STEVE in the archived data accessible on that website. These events have a unique characteristic, distinct from STEVE; they were observed poleward of the bright green arc in the post-midnight sector. In this study, we examine two cases (Events 1 and 2) of such optical phenomena by considering their similarity/dissimilarity to STEVE and discuss the conditions required for the phenomena to occur by combining data from LEO satellites, commercial digital cameras, and a narrow-band multi-wavelength ASC.

Instruments

Digital cameras

Since September 2011, a commercial all-sky digital camera has been operative at Ramfjordmoen Research Station in Tromsø, Norway (69.6°N, 19.2°E). Nikon D7200 and Sigma 4.5 mm f/2.8 EX DC HSM Circular Fisheye lens were used for Event 1. Nikon D5000 with the same lens was used for Event 2. The temporal resolution, exposure duration, and ISO sensitivity were, respectively, 30 s, 8 s, and 3200 for Event 1, were, respectively, 1 min, 15 s, and 2500 for Event 2. The original JPEG images have a size of 4496×3000 pixels.

Day/night band of VIIRS onboard NOAA-20

This study uses the imaging data from the day–night band (DNB) of the Visible Infrared Imaging Radiometer Suite (VIIRS) onboard the NOAA-20 satellite (Cao et al. 2018). VIIRS is a group of imagers capturing the Earth's surface from the low-Earth orbit (833 km at apogee) with 22 bands: five I-bands, 16 M-bands, and DNB (Lee et al. 2006). Most I- and M-bands have a narrow bandwidth (20–80 nm), distributing in 400–1200 nm. By contrast, DNB is sensitive to a wide visible band: 500–900 nm, and the dynamic range is from 3×10^{-9} to 2×10^{-2} W cm^{-2} str^{-1}; thus, it can detect faint emission during the night. The spatial resolution of DNB is 0.75 km, and the swath width is 3000 km (Miller et al. 2013). The geolocation data provide the latitude, longitude, and sea level height. Assuming the auroral emission layer to be distributed at 100 km altitude, we determined coordinates at 100 km by calculating the intersection between a line-of-sight vector and a spheroid with a radius of $R_E + 100$ km. Here, R_E represents the World Geodetic System 1984 (WGS84) radius. Moreover, moonlight contamination was subtracted from the measured radiance with the empirical model (Zinke 2017).

Swarm satellites

Swarms are polar-orbiting LEO satellites. This study uses data from the electric field instrument (EFI) onboard Swarm A and B. The EFI contains a pair of Langmuir probes which provide spacecraft potential, electron density, and electron temperature with a temporal resolution of 0.5 s. The ion drift is derived by two thermal ion imager sensors (Knudsen et al. 2017). The data are given in the cross-track coordinate system. The x-axis is the direction of the satellite motion, the y-axis is perpendicular to the x-axis and right to the direction of the satellite motion, and the z-axis is downward, completing the right-handed system configuration. The y-axis direction is approximately aligned with the east–west direction since the Swarms are polar-orbiting satellites.

OMTI

Optical mesosphere thermosphere imager (OMTI) was installed at the same research station as the digital cameras (Shiokawa et al. 1999). OMTI captures all-sky images at five different lines, i.e., 557.7 nm (the green line), 630.0 nm (the red line), 720.0 nm (OH), 732.0 nm (O^+), and 572.5 nm (background), by rotating a filter wheel. The temporal resolution was 70–180 s for the auroral lines and 8 min for the background line. Comparing the all-sky images at the auroral (i.e., green and red) and background (572.5 nm) lines makes it possible to estimate whether an optical phenomenon is an aurora or not. The optical calibration to derive the absolute optical intensity in Rayleigh was conducted with an integrating sphere installed at the National Institute of Polar Research, Tokyo, Japan (Ogawa et al. 2020), on 20th October 2008.

Observational results

Event 1 on 28th December 2021

Event 1 occurred when geomagnetic and solar wind conditions were not significantly disturbed. Figure 1a shows the H component of the SYM index for 5 days, including Event 1. The minimum SYM-H was −30 nT during 5 days, and no significant magnetic storms were observed. Panels b–e are the interplanetary magnetic field (IMF), solar wind speed, proton density, and dynamic pressure from the dusk of the 27th to the dawn of the 28th of December 2021. The z component (shown in red) of IMF (IMF B_z) was negative during 17–18 UT and 03–06 UT, but the rest of the time, it was positive or near zero, and the intensity (shown in black) was ~10 nT, implying no significant disturbance. The solar wind speed was also moderate at about 400 km/s. The proton density and dynamic pressure showed a transient increase in 14–16 UT but no remarkable variation afterward.

Panel (f) shows the upper (black) and lower (red) of the SuperMAG index (Gjerloev 2012). The substorm activities were observed at around 19 and 01 UT with a minimum SML lower than −250 nT. Panel g is a north–south keogram of the color images from the digital camera installed in Tromsø, Norway. Comparing panels (f) and (g), we can see the auroral appearance in 17–20 UT and 23–03 UT, responding to the substorm activities shown in panel (f). Shortly after the negative bay in SML, a purple glow was observed in the late growth phase, as indicated by the white arrow. The period indicated by the white dotted lines is enlarged in Fig. 2 for a more detailed analysis.

The purple glow was observed in the late growth phase of the substorm. The upper panel of Fig. 2 is an enlarged keogram for the period indicated by the white dashed lines in Fig. 1g. The purple glow appeared for less than 10 min in the cross section of the keogram (geographic north to south) with the southward propagation of the green aurora before the auroral breakup (i.e., poleward expansion) at 01:19 UT, i.e., optical data also show that it appeared in the late growth phase of the substorm.

The purple glow was an arc-shaped phenomenon extending in the east–west direction and appeared northward (poleward) of the green discrete arc. Eight all-sky images are displayed in the lower panels. The captured times are labeled and shown on the top of the keogram. A green aurora was not bright in panel (a), and no purple glow was seen. At this time, Swarm B flew on the trajectory indicated by the yellow arrow. Panels b–d were captured every 30 s, and the white arrows indicate that the bright greenish region drifted eastward (toward the morning side) at ~4 km/s if we assume the emission layer was 100 km altitude. The green aurora got brighter and formed the arc shape in panel (e). The purple glow was observed on the eastern edge (enlarged in the lower left), but there was optical pollution from Tromsø city on the western side; thus, it is unclear if it appeared from the eastern side only from these snapshots. In panel (f), the purple arc appeared broadly in the east–west direction simultaneously and was located poleward of the green arc. The purple arc was brightest in panel (g) and as bright as the green arc. It disappeared several minutes later (at 01:07 UT), and then only the wavy discrete auroras were observed in panel (h), leading to the auroral breakup. Diffuse (pulsating) auroras were observed after the breakup.

The 30-s temporal resolution of the digital camera was not high enough to identify the direction of longitudinal progression, but the video of all-sky images attached as Additional file 1 visualizes the eastward drift motion of the fine structure of the purple arc. Specifically, as shown in Additional file 2, the purple arc had a fading area in brightness, which propagated eastward. From the right panels of these images projected at 100 km, 200 km, and 300 km altitudes, the propagation velocity of the structure can be estimated to be around 4 km/s, 6 km/s, and 10 km/s at the assumed altitudes, respectively. The video from a high-speed camera installed near the digital camera (also attached as Additional file 3) showed that the purple arc had emissions at 844.6 nm and its intensity was lower than that of the green arc in the south. In addition, in Additional files 1, 2, it can be confirmed that the fine structure of the green aurora immediately south of the purple arc propagates together with the propagation of the fading area of the purple arc.

In Event 1, NOAA-20 flew over the Lapland, and the DNB observation covered a wide area, as shown in the black-and-white image in Fig. 3. The area shown in Fig. 3 was scanned from 00:50 to 00:55 UT from the high latitude side. In particular, the green arc and purple arc were

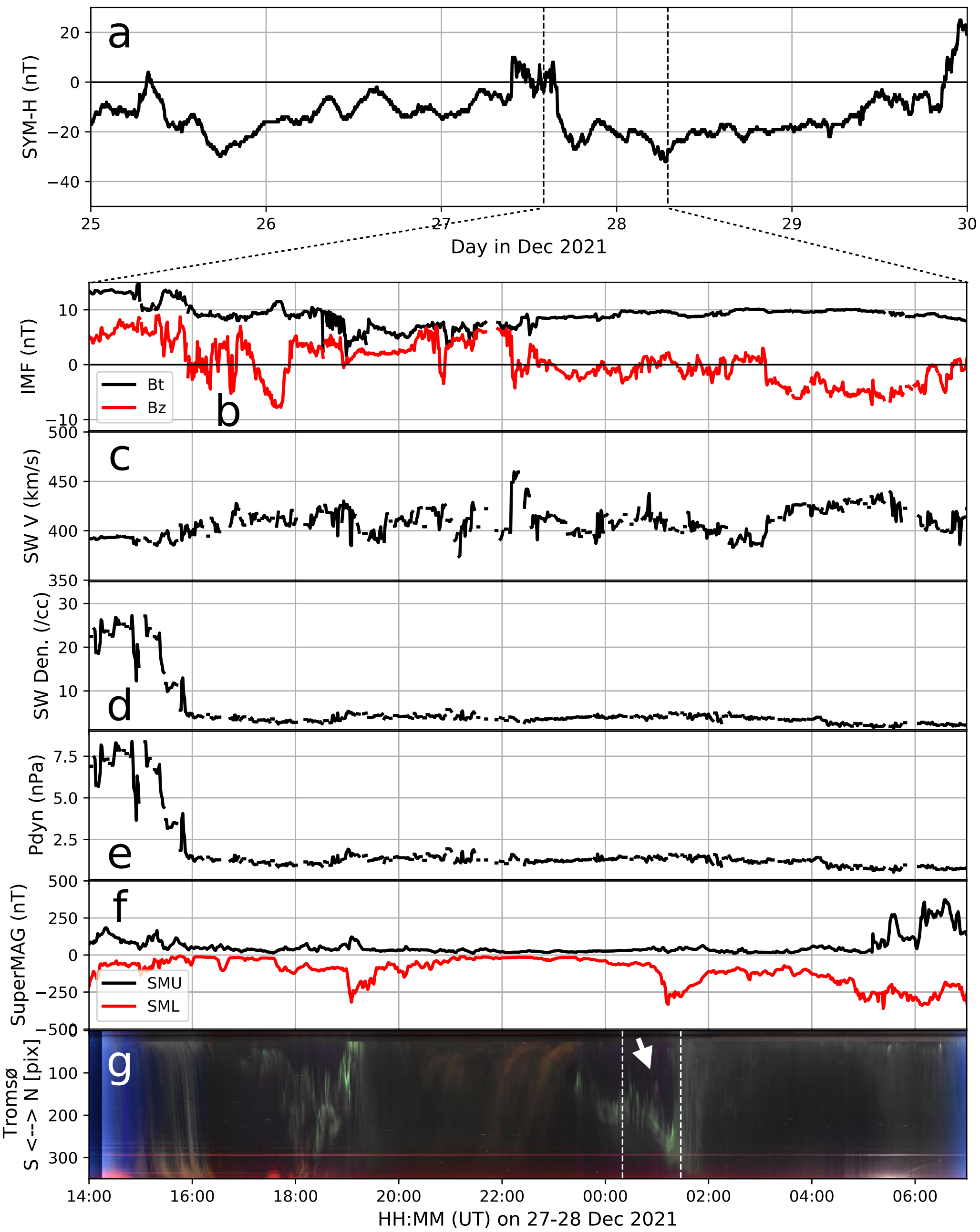

Fig. 1 Solar wind and geomagnetic conditions during Event 1. **a** H component of the SYM index from 25th to 30th December 2021. The dashed lines mark the period shown in panels **b**–**g**. **b** Intensity (black) and *z* component (red) of the interplanetary magnetic field (IMF). **c** Speed of the solar wind (SW). **d** Solar wind density. **e** Solar wind dynamic pressure. **f** SuperMAG SMU and SML indices: upper (black) and lower (red). **g** North–south keogram from dusk to dawn derived from the digital camera installed in Tromsø, Norway

scanned at around 00:54 UT. The moonlight contamination was subtracted from the original radiance with the empirical model (Zinke 2017). Comparing the DNB image with the overplotted color image from the ground-based digital camera, we can identify the arc indicated by the white arrows as the purple arc. The purple arc has a broad longitudinal structure and is distributed from 1.5 to 3.5 MLT, i.e., at least 1000 km long. The blue and yellow arrows are the trajectories of Swarm A and B, respectively, labeled with diamonds and time (UT) every 30 s. As shown in Fig. 2a, Swarm B passed above Tromsø about 20 min before the appearance of the purple arc. Swarm A flew over the auroral latitudes during the appearance of the purple arc, although it was outside

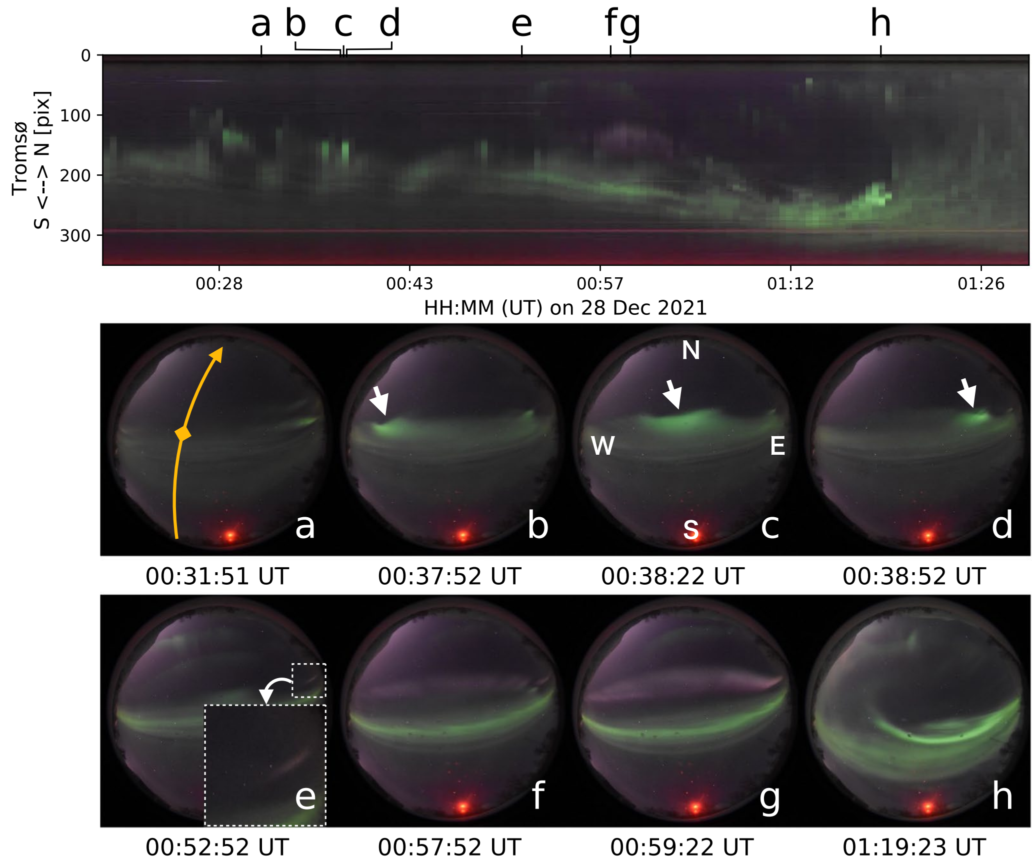

Fig. 2 (Top) Close-up of the keogram shown in Fig. 1g. Panels **a**–**h** correspond to the derived time of the bottom eight snapshots. **a**–**h** Snapshots from the all-sky digital camera in Tromsø. The top is north, and the right is east. The yellow arrow in **a** is the apparent trajectory of Swarm B. The yellow diamond indicates the location at 00:32:00 UT. The white arrows in panels **b**–**c** guide the eastward motion of the discrete aurora. The bottom left in panel **e** is a close-up of the dashed small square region in the east

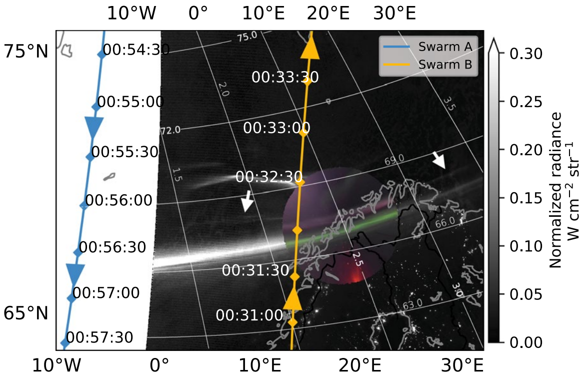

Fig. 3 Projection of the DNB image and all-sky image to 100 km altitude. Both the purple and green arcs extended east–west widely. White arrows guide the continuity of the purple arc in the DNB image. Blue and yellow arrows indicate the trajectories of Swarm A and B, respectively. White grid lines show the AACGM latitude and local time

of the field of view of the optical observations. In other words, the simultaneous observation with optical instruments and satellites was not perfect spatially for Swarm A and temporally for Swarm B.

Although the spatiotemporal conjugacy was not desirable, measurements from Swarms suggest that the purple arc was distributed on the R1 side of the boundary between R1 and R2 FACs. Figure 4 summarizes the in-situ observations from Swarm A (left) and Swarm B (right). The panels are, from top to bottom, the east–west components of the ion drift (positive is eastward), IGRF-subtracted magnetic field, the electron temperature, and the electron density. The periods when Swarms pass over the purple and green arcs are roughly hatched in purple and green, respectively, by comparing with Fig. 3. The drift speed was as fast as ~2.5 km/s in the purply hatched period in both cases, but in the case of Swarm A, a steep drop in speed, a characteristic of DAPS (Liu et al. 2020), was observed near the boundary between purple and green regions. Comparing panels (a) and (e), panel (a) shows a stable westward drift in equatorward (~1.0

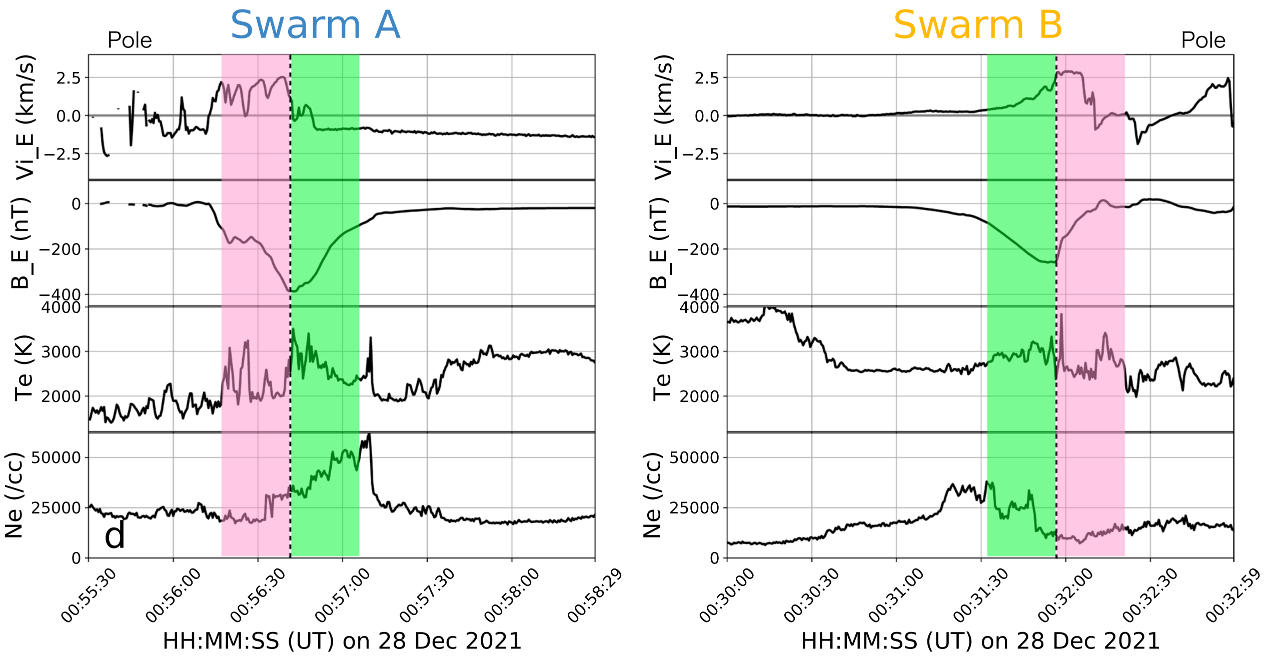

Fig. 4 Measurements by Swarm A **a**–**d** and B (**e**–**f**. (**a**, **e** East–west ion drift speed. The positive value indicates the eastward flow. (**b**, **f** East–west magnetic variation. The positive gradient corresponds to the upward FAC. The dipole component was subtracted by the IGRF model. (**c**, **g** Plasma temperature. (**d**, **h** Plasma density. The estimated purple and green arcs regions are hatched in purple and green, respectively

km/s). This suggests that there was a westward bias in the measurements and that the eastward ion flow in the purple hatched region may actually be a few km/s faster than the values in panel (a). The drift direction was eastward (positive value in panels), which is opposite to STEVE, but it is natural since the return flow of the dawnside convection cell is eastward. By applying Ampere's law to the east–west component of the geomagnetic field, we can determine the direction of FAC and find that the purple arc was in the region of downward FAC (R1) while the green arc was in the region of upward FAC (R2). The geomagnetic field variation was about 300 nT. Several spikey peaks above 3000 K were detected in the plasma temperature during the purple hatched period, but the value was not significantly different from those in the green arc. The electron density was about 20,000 /cc in panel d and 11,000 /cc in panel h, both of which were half those of the green arc.

Event 2 on 13th November 2012

The glow showing a similar color to Event 1 appeared on the poleward side of the bright green arc in the post-midnight sector on 13th November 2012. In this case, there was no conjunction with LEO satellites, but multi-wavelength all-sky images by OMTI installed at the same observatory were available. The solar wind and geomagnetic indices during this event are shown in Fig. 5 in the same format as Fig. 1. Unlike Event 1, this case occurred during the main phase of a major magnetic storm with a SYM-H minimum reaching −100 nT, as shown in panel (a). The IMF B_z was continuously negative from 18 UT until dawn, as shown in panel (b). It further weakened from 00 UT and sometimes reached −20 nT. The solar wind speed was slow, below 400 km/s. The proton density and dynamic pressure had enhanced from 23 UT. SML was below −500 nT during most of the time from 19 UT, i.e., the geomagnetic field was highly disturbed compared to Event 1. It is difficult to identify the phase of the substorm, but SML further decreased from 23 UT with the enhancement of solar wind parameters. The auroral activity was continuously active throughout the night, as seen in panel (g). Purple/pink patchy signatures were observed, indicated by the white arrows.

Figure 6 is a minute-by-minute sequence of color all-sky images at times indicated by the white arrows in Fig. 5g. Tromsø was located at about 0.6 MLT in this interval. In panels a–h, the white and yellow arrows on the poleward of the green discrete aurora guide the eastward propagation of pink/purple patches, and its speed was at about 2 km/s. The discrete green aurora also propagated eastward as guided by the green arrows. This characteristic, where the green aurora and purple glow propagate together, was also observed in Event 1 (see Additional files 1, 2). In the area poleward of the patches, several ray structures were seen.

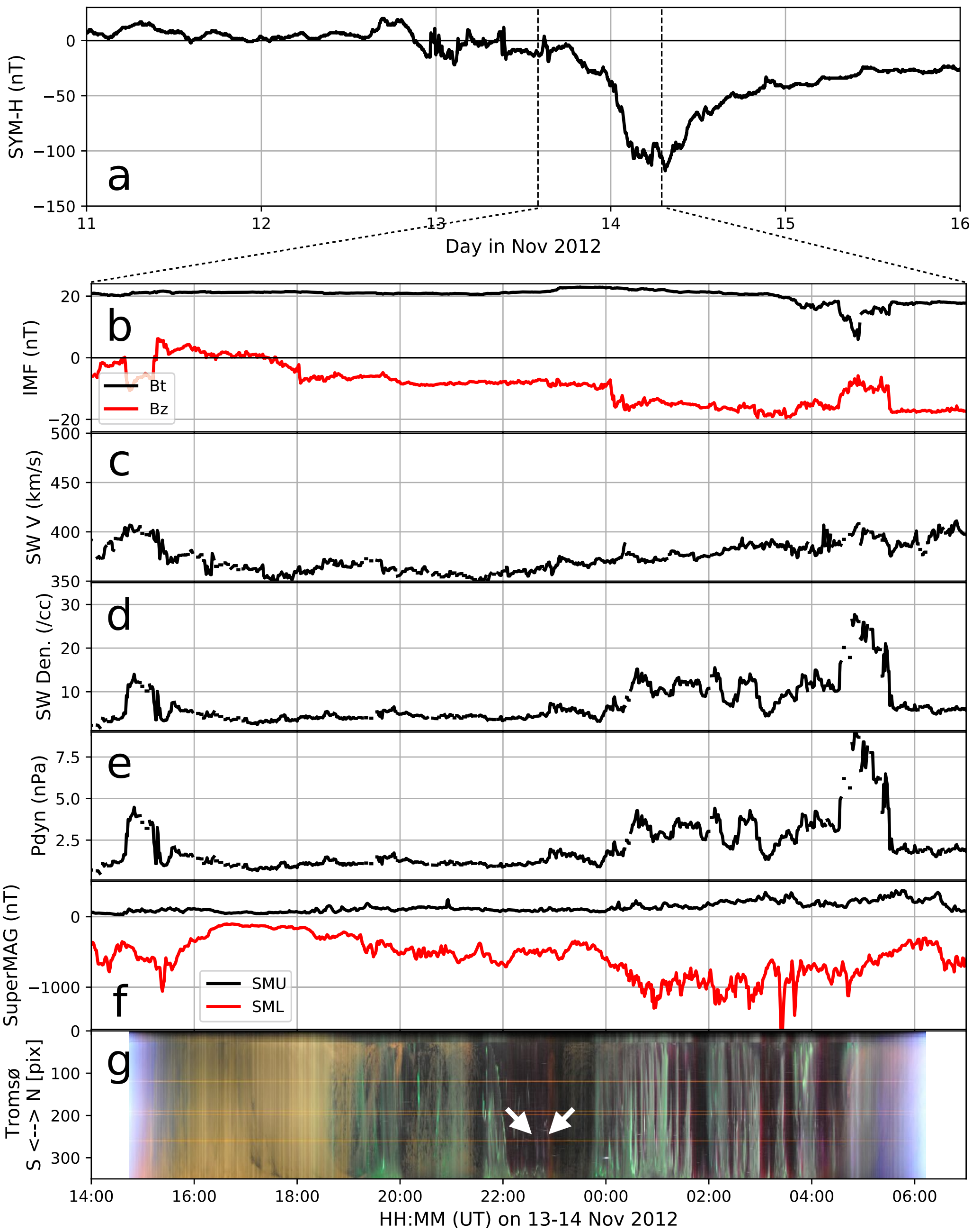

Fig. 5 Geomagnetic conditions during Event 2. The format is the same as in Fig. 1. **a** H component of the SYM index from 11th to 16th November 2012. The dashed lines mark the period shown in panels **b**–**g**. **b** Intensity (black) and z component (red) of the interplanetary magnetic field. **c** Speed of the solar wind. **d** Density of the solar wind plasma. **e** Solar wind dynamic pressure. **f** SuperMAG index upper (black) and lower (red). **g** North–south keogram from dusk to dawn derived from the digital camera installed in Tromsø, Norway. The white arrows indicate the purple patches. Figure 6 shows the snapshots around this time

During this interval, multi-wavelength data from OMTI was available, and panels i–l are narrow-banded images: green line (557.7 nm), red line (630.0 nm), O^+ line (732.0 nm), and background line (572.5 nm). As indicated by the white arrows, the purple/pink patches are detected at all the wavelengths, including the background line. The background line contains no specific emissions of aurora/airglow; thus, the southern discrete aurora and ray structures were not seen in panel (l). Consequently, the purple/pink patches are might have different spectrum from auroras.

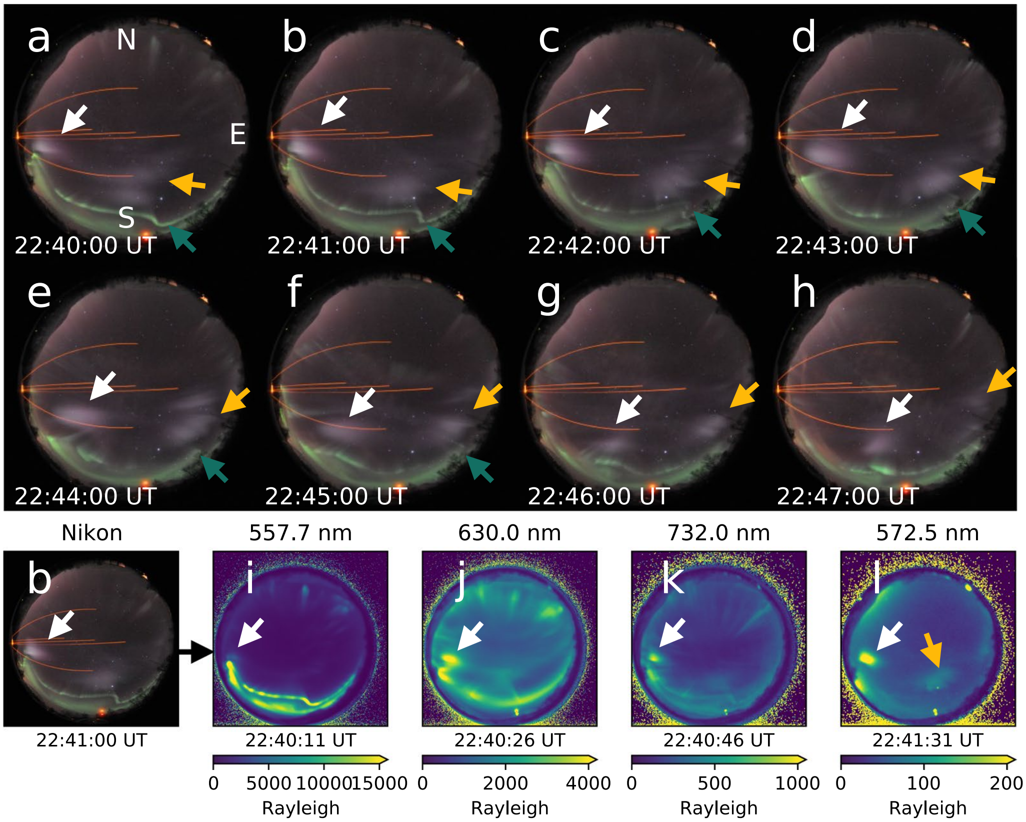

Fig. 6 (**a**–**h**) Snapshots by the digital camera from 22:40:00 to 22:47:00 UT. The top is north, and the right is east. Several purple patches appeared poleward of the wavy discrete aurora. The white and yellow arrows guide the eastward propagation of the patches. The green arrows guide the eastward propagation of the wavy structure of the discrete aurora. **i**–**l** All-sky images observed from OMTI at the closest time to (**b**). The measured wavelengths are at the top of each panel. The recorded times are at the bottom. The color scale indicates the Rayleigh value. The white and yellow arrows indicate that the purple patch has an emission at all four wavelengths, including the background line at 572.5 nm

Discussion

The characteristics of the purple arc in Event 1 are summarized as follows:

- It appeared in the late growth phase of the substorm, which has a minimum SML of −250 nT without a significant magnetic storm. The arc was distributed northward (poleward) of the southward-moving green discrete arc.
- It exhibited a longitudinal length of at least 1000 km and was on the R1 side (downward FAC) of the boundary between R1 and R2.
- A sudden depletion in the ion speed at the R1/R2 boundary, a characteristic signature of DAPS, was not observed prior to the purple arc's appearance but was observed during its appearance.
- Although there was no significant difference in the electron temperature between the purple and green arcs, the electron density decreased within the purple arc.

Similarities between STEVE and purple arc are color, broad longitudinal elongation, low electron density, and their occurrence within the downward FAC region. Dissimilarities are their location relative to the auroral oval (poleward part of it or equatorward), MLT, the direction of the ion drift, the phase of substorms, and the difference in the electron temperature as compared to the auroral oval (MacDonald et al. 2018; Nishimura et al. 2023b).

The purple arc in Event 1 has a similar color to STEVE. In the polar region, however, several optical phenomena (i.e., aurora/airglow) exist, other than STEVE, showing non-green colors. Auroras caused by the resonance scattering are often captured as purple glows during sunset/sunrise periods. This color is due to the band emission of nitrogen molecules ions excited by the solar illumination at higher altitudes (Shiokawa et al. 2019). Both Events 1 and 2 were observed at least 5 h before sunrise and the shadow hight was about 1800 km; thus, the resonance scattering is not the driver of the present purple emissions. The purple glow can also be caused by the band emissions of nitrogen molecules and nitrogen molecular ions due to precipitation of high-energy (>30 keV) electrons to altitudes below 100 km. Since no green glow is visible in the purple arc, this scenario would require almost no precipitation of medium-energy electrons responsible for the 557.7 nm emission. On the other hand, the purple arc has emissions at 844.6 nm, which must be caused by low-energy electrons. This means that there were almost no electrons in the medium energy band that caused the 557.7 nm emission, and only high- and low-energy electrons precipitated into this region if this purple glow is caused by precipitating electrons. However, this scenario is not likely because precipitating electrons can cause visible 557.7-nm auroral emission in a rather broad energy range from 0.8 to 10 keV (e.g., Banks et al. 1974). Stable auroral red (SAR) arc (Gallardo-Lacourt et al. 2021) and ephemeral red arc (Oyama et al. 2020), which has emissions at 630.0 nm, should be reddish in digital images. Moreover, SAR arc is more pronounced in the sub-auroral region, which is different from the location of our events. In one of the events in Liu et al. (2020), proton precipitation was observed with DAPS. The characteristics of proton auroras are distinctively different from our cases, which showed only purple/pink glow, while proton auroras are generally accompanied by the green line emission produced by the secondary electrons.

Although it is unclear whether Event 2 was triggered by the same mechanism as Event 1, besides the similarity in color, Event 2 appeared similar location to Event 1, i.e., poleward of the green arc in the post-midnight sector. The propagation direction of the purple arc was eastward, which is shown in the movie from the digital camera and also in the images from the high-speed (EMCCD) camera installed in the same location, available as Additional files 1, 3. Events 1 and 2 exhibited the same propagation direction, consistent with those of the green auroras. Events 1 and 2 have several similarities, suggesting that there is a common mechanism responsible for triggering the purple arc and the patches.

The optical phenomenon documented in this study may be a visual manifestation of DAPS and the dawnside counterpart of STEVE. Figure 7a illustrates the difference in location between STEVE and the purple arc. Both phenomena appear in a region of downward FACs and low conductivity, although those appear in different local time sectors. DAPS, the dawnside counterpart of SAPS, is generated in the region where our events were observed. According to Liu et al. (2020), a possible generation mechanism of DAPS is as follows: 1) the geomagnetic field becomes disturbed, and R2 FAC is enhanced as the plasma sheet pressure increases; 2) to keep the

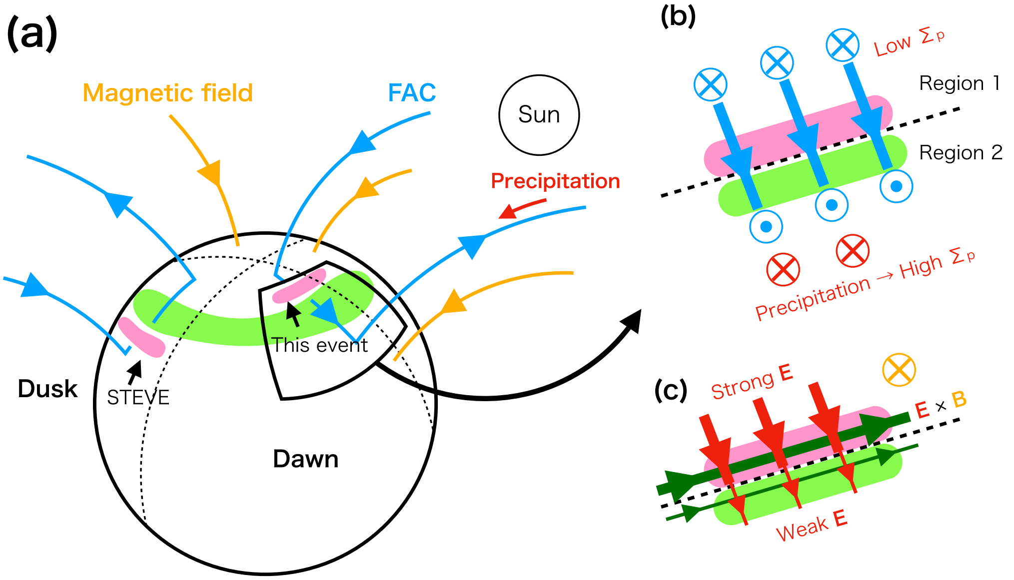

Fig. 7 **a** Schematic illustration showing the relative location of STEVE and phenomena reported in this paper. The circle is the Earth, and the green region is an auroral oval. STEVE appears pre-midnight and equatorward of the oval, while our events were found post-midnight and poleward part of the oval. The blue arrows show FAC and Pedersen current. The yellow arrows show the geomagnetic field lines. **b**–**c** Possible generation mechanism of DAPS and the purple glow. **b** The difference in the number of careers (electrons) makes the spatial gradient of the conductivity. **c** Spatial gradient of the conductivity makes a strong electric field in Region 1, especially near the boundary between Regions 1 and 2. The strong electric field makes a fast eastward drift speed

current continuity, southward Pedersen current and R1 FAC are intensified; 3) a latitudinal gradient of the conductivity is generated because only R2 has precipitation of sufficient electrons; 4) the polarization electric field is enhanced near the R1/R2 boundary to keep the current continuity. This process enhances the eastward $\mathbf{E} \times \mathbf{B}$ drift and then forms DAPS. The drift speed is the largest on the R1 side of the R1/R2 boundary since the electric field is most intensified in this region. This area corresponds to the purple hatched region in Fig. 4, where the purple arc was observed. This allows us to suggest that the purple arc is an optical signature/manifestation of DAPS. Since DAPS is the dawnside counterpart of SAPS/SAID, the purple arc might be the dawnside counterpart of STEVE. Note that the difference in the drift direction between SAPS and DAPS in Fig. 4 originates from the difference in the flow of the convection cell.

Event 1 occurred during the late growth phase of an isolated substorm. Event 2, in contrast, occurred during a highly disturbed period, including multiple substorms when the phase of each substorm cannot be identified. Nevertheless, the SML was further reduced from 1 h after the appearance of the purple glow, and hence the plasma sheet pressure might have been intensified, similar to the late growth phase. In the model proposed by Liu et al. (2020), DAPS may appear more frequently during the late growth phase because the enhancement of R2 FAC with increasing the plasma sheet pressure is necessary to form DAPS. DAPS has been observed in all the substorm phases: the growth (Jiang et al. 2015), expansion (Liu et al. 2020), and recovery phases (Liu et al. 2018), although its statistical tendency is still unclear. Both the purple glow and STEVE do not necessarily require a strong geomagnetic disturbance, as in Event 1, but STEVE/SAID is mainly observed during the recovery phase (Anderson et al. 1993; Nishimura et al. 2023b). It is essential to compare the timings of occurrence between STEVE and the purple arc for a detailed understanding of the emission mechanism.

Plasma instabilities might have made the purple glow patchy during Event 2. In both events, the green discrete auroras appeared on the lower latitude side (equatorward) of the purple glow. When the purple glow showed a stable arc shape, the shape of the discrete aurora was also stable (Event 1). By contrast, when the purple glow exhibited a patchy shape, the discrete aurora at the lower latitude showed a wavy form (Event 2). During Event 2, the geomagnetic field was highly disturbed, as shown in Fig. 5. In such a situation, the injected plasma might have a complex distribution in the longitudinal direction, leading to the occurrence of interchange instabilities, for example, the Ballooning instability producing auroral beads (Motoba et al. 2012; Kalmoni et al. 2018). Liu et al. (2020) has also suggested that the steep latitudinal gradient of DAPS flow may trigger Kelvin–Helmholtz instability which has the potential to cause the structuring of glow into patches. Regardless of the generation mechanisms, during Event 2, STEVE-like purple glow was surely observed in the post-midnight sector in the form of patches, suggesting that similar patch-shaped STEVE could also be observed on the duskside in the sub-auroral latitudes.

The generation mechanism of STEVE still remains unveiled. Based on its continuous spectrum and the relationship with fast ion flow, however, it may be produced by the chemical reaction between O and NO generated by the vibrationally excited nitrogen molecules (Gillies et al. 2019; Mende et al. 2019; Harding et al. 2020; Mishin and Streltsov 2022). This reaction indeed requires fast ion flows. A fast flow of 2.5 km/s was actually observed during Event 1 in the purple hatched area in Figs. 4a and 4e. Although the threshold speed required for the emission is unclear and the values in Fig. 4a may have a few km/s westward bias, the value of 2.5 km/s would be sufficient to generate such thermal emissions because STEVE was observed with a 3.0 km/s flow in Nishimura et al. (2020) (see their Fig. 2n). However, Nishimura et al. (2023a) recently reported that STEVE has fine-scale (several to a few tens of km) structures, which are not likely to be produced by the reaction of O and NO. Event 2 also had the patchy structure; thus, the generation mechanism of our cases needs to be clarified. Worth mentioning, the values of the ion drift speed plotted in Figs. 4a and 4e were almost similar. However, a steep depletion in the speed was seen at the R1/R2 boundary only in Fig. 4a. Data plotted in Fig. 4a were obtained during the appearance of the purple arc, while those plotted in Fig. 4e were observed during the absence. This implies that not only the ion drift speed itself but also the spatial gradient of the ion drift played a critical role in generating the emission. Of course, there is a possibility that faster flow existed within the purple arc over Tromsø, considering the trajectory of Swarm A was outside the field of view of the optical observations. Furthermore, the localized co-propagation of the green aurora and purple glow in both events may suggest that the current system forming the purple glows is controlled by fluctuations in the mesoscale electron precipitation regions rather than by the large-scale convection cell in the ionosphere.

One of the reasons for the late discovery of the current purple glow compared to STEVE may be the difference in the characteristics of the low-conductance regions creating SAPS and DAPS. As discussed by Liu et al. (2020), the low-conductance region that produces SAPS is a mid-latitude trough formed by the ionospheric convection. In comparison, the region of low-conductance that produces DAPS is located in the poleward part of the auroral oval; thus, the conductivity is relatively higher. Therefore, a rapid ion flow and corresponding steep gradient would be less likely to be produced in the post-midnight than in the pre-midnight sector. This implies that the purple glow in the post-midnight sector is less frequent than STEVE in the pre-midnight sector.

The local time and latitudinal dependence of citizen scientists' activity could also be a reason for the delayed discovery of the phenomena. STEVE is typically observed in the pre-midnight sector, where dynamic discrete auroras frequently occur. In addition, STEVE has been captured in the sub-auroral region, a more populated region in general. By contrast, the purple glow was observed in the post-midnight sector, where dynamic auroras are less frequent. More importantly, the purple glow was observed at higher latitudes than the bright green arc. Thereby, probably fewer citizen scientists are chasing auroras in such high-latitude regions. Commercial color digital cameras have become one of the essential observation equipment because they are inexpensive and can provide color information easily, i.e., without any special post-processing. Even in regions where photographers are less likely to be active, as in the current cases, the digital camera played an indispensable role in discovering a new phenomenon. Therefore, not only photographers but also researchers should routinely continue their digital camera observations.

Conclusions

We observed STEVE-like-color phenomena on the poleward part of the auroral oval in the post-midnight sector with a commercial digital camera. We have reported two cases; one showed arc-like, and the other showed patchy structure. A stable green discrete auroral arc accompanied the arc-like one, and wavy discrete auroras accompanied the patchy case on its equatorward. In-situ data obtained by Swarm satellites were available when the arc-like one was observed although the spatiotemporal conjugacy was not ideal. The magnetic field data suggested that the purple arc appeared on the R1 side of the boundary between R1/R2 FACs. An eastward fast ion drift (∼ 2.5 km/s) was also observed near the purple glow. The ion flow had a strong gradient near the R1/R2 boundary, a characteristic of the dawnside fast ion flow called DAPS. Since STEVE is an optical phenomenon related to SAID/SAPS and DAPS is the dawnside counterpart of SAPS, the optical phenomena reported here may be the dawnside counterpart of STEVE and the optical manifestation of DAPS.

Abbreviations

STEVE	Strong thermal emission velocity enhancement
SAID	Subauroral ion drift
SAPS	Subauroral polarization stream
DAPS	Dawnside auroral polarization stream
THEMIS	Time History of Events and Macroscale Interactions during Substorms
ASC	All-sky camera
LEO satellite	Low-Earth orbiting satellite
FAC	Field-aligned current
DNB	Day–night band
VIIRS	Visible Infrared Imaging Radiometer Suite
EFI	Electric field instrument
OMTI	Optical mesosphere thermosphere imager
IMF	Interplanetary magnetic field
MLT	Magnetic local time

Supplementary Information

The online version contains supplementary material available at https://doi.org/10.1186/s40623-024-01995-9.

Additional file 1. Video of the all-sky images from the all-sky digital camera.

Additional file 2. The original all-sky images from the digital camera and projections of those images.

Additional file 3. Video of the all-sky images from the high-speed (EMCCD) camera.

Acknowledgements

The authors thank David Knudsen and Johnathan Burchill for giving comments on the results from the Swarm satellites. The authors thank the EISCAT staff for operational assistance at Ramfjormoen Research Station in Tromsø, Norway. This study was supported by the Japan Society for the Promotion of Science (JSPS) KAKENHI Grant Numbers 21J20254, 22H00173, 21KK0059, 20K20940, 15H05747, 21H04516, and 21H04518. The first author is a Research Fellow DC of JSPS. This work was carried out by the joint research program of the Institute for Space-Earth Environmental Research (ISEE), Nagoya University. We gratefully acknowledge the SuperMAG collaborators (https://supermag.jhuapl.edu/info/?page=acknowledgement). We used the Inter-university Upper atmosphere Observation NETwork (IUGONET) database (IUGONET Type-A) (Tanaka et al. 2023) for OMTI imager data analysis at Tromsø.

Author contributions

SNanjo conducted the overall analysis and wrote most part of the manuscript. GH surveyed the past observation data and identified the events. AS calculated the Rayleigh value of the images obtained by OMTI. SNozawa installed and maintained the digital cameras. KS installed, maintained, and calibrated OMTI. KH made a video by the EMCCD camera attached as Additional file 3 and supervised the study. AS, KS, SNozawa, and KH discussed the results and interpreted them with the first author, and revised the manuscript. All authors read and approved the final manuscript.

Funding

This study was supported by the Japan Society for the Promotion of Science (JSPS) KAKENHI Grant Numbers 21J20254, 22H00173, 21KK0059, 20K20940, 15H05747, 21H04516, and 21H04518.

Availability of data and materials

Images from the digital camera for a specific date in the past can be obtained by giving an 8-digit number in the format of YYYYMMDD. For example, images on 26 January 2022 are available at https://www.isee.nagoya-u.ac.jp/~eiscat/obs/d5000/html/pre20220126.html. The data from the Swarm satellites can be downloaded from https://swarm-diss.eo.esa.int/. The DNB image from the NOAA20 satellite can be downloaded from https://sips.ssec.wisc.edu/. The SuperMAG indices can be downloaded from https://supermag.jhuapl.edu/indices/. The OMNI data can be downloaded from https://omniweb.gsfc.nasa.gov/. The all-sky images from OMTI can be downloaded from https://ergsc.isee.nagoya-u.ac.jp/data/ergsc/ground/camera/omti/asi/.

Declarations

Competing interests

The authors declare that they have no competing interests.

Author details

[1]The University of Electro-Communications, Tokyo 182-8585, Japan. [2]Photographer, Tromsø, Norway. [3]Institute for Space-Earth Environmental Research, Nagoya University, Aichi, Japan. [4]Swedish Institute of Space Physics (IRF), Kiruna, Sweden.

Received: 4 September 2023 Accepted: 19 March 2024
Published online: 09 April 2024

References

Anderson PC, Hanson WB, Heelis RA, Craven JD, Baker DN, Frank LA (1993) A proposed production model of rapid subauroral ion drifts and their relationship to substorm evolution. J Geophys Res Space Phys 98(A4):6069–6078

Anderson PC, Carpenter DL, Tsuruda K, Mukai T, Rich FJ (2001) Multisatellite observations of rapid subauroral ion drifts (said). J Geophys Res Space Phys 106(A12):29585–29599

Archer WE, St-Maurice J-P, Gallardo-Lacourt B, Perry GW, Cully CM, Donovan E, Gillies DM, Downie R, Smith J, Eurich D (2019) The vertical distribution of the optical emissions of a steve and picket fence event. Geophys Res Lett 46(19):10719–10725

Banks PM, Chappell CR, Nagy AF (1974) A new model for the interaction of auroral electrons with the atmosphere: spectral degradation, backscatter, optical emission, and ionization. J Geophys Res 79(10):1459–1470

Cao C, Blonski S, Wang W, Uprety S, Shao X, Choi J, Lynch E, Kalluri S (2018) NOAA-20 VIIRS on-orbit performance, data quality, and operational Cal/Val support. In: Xiong X, Kimura T (eds) Earth observing missions and sensors: development, implementation, and characterization. International Society for Optics and Photonics, SPIE, Bellingham

Chu X, Wolter L, Malaspina D, Andersson L, Connors M, Chatfield C, Zeller N (2020) Morphological characteristics of strong thermal emission velocity enhancement emissions. J Geophys Res Space Phys 125(12):e2020JA028110

Foster JC, Vo HB (2002) Average characteristics and activity dependence of the subauroral polarization stream. J Geophys Res Space Phys 107:10–16

Gallardo-Lacourt B, Nishimura Y, Donovan E, Gillies DM, Perry GW, Archer WE, Nava OA, Spanswick EL (2018) A statistical analysis of steve. J Geophys Res Space Phys 123(11):9893–9905

Gallardo-Lacourt B, Frey HU, Martinis C (2021) Proton aurora and optical emissions in the subauroral region. Space Sci Rev 217(1):10

Galperin YI, Ponomarov YN, Zosinova AG (1973) Direct measurements of ion drift velocity in the upper ionosphere during a magnetic storm. Cosmicheskie Issled. 11:273

Gillies DM, Donovan E, Hampton D, Liang J, Connors M, Nishimura Y, Gallardo-Lacourt B, Spanswick E (2019) First observations from the trex spectrograph: the optical spectrum of steve and the picket fence phenomena. Geophys Res Lett 46(13):7207–7213

Gjerloev JW (2012) The supermag data processing technique. J Geophys Res Space Phys 117(A9)

Gkioulidou M, Wang C-P, Lyons LR, Wolf RA (2009) Formation of the harang reversal and its dependence on plasma sheet conditions: Rice convection model simulations. J Geophys Res Space Phys 114(A7)

Harding BJ, Mende SB, Triplett CC, Wu Y-JJ (2020) A mechanism for the steve continuum emission. Geophys Res Lett 47(7):e2020GL087102

Iijima T, Potemra TA (1976) The amplitude distribution of field-aligned currents at northern high latitudes observed by triad. J Geophys Res 81(13):2165–2174

Jiang F, Kivelson MG, Strangeway RJ, Khurana KK, Walker R (2015) Ionospheric flow shear associated with the preexisting auroral arc: a statistical study from the fast spacecraft data. J Geophys Res Space Phys 120(6):5194–5213

Kalmoni NME, Rae IJ, Watt CEJ, Murphy KR, Samara M, Michell RG, Grubbs G, Forsyth C (2018) A diagnosis of the plasma waves responsible for the explosive energy release of substorm onset. Nature Commun 9(1):4806

Karlsson T, Marklund GT, Blomberg LG, Mälkki A (1998) Subauroral electric fields observed by the freja satellite: a statistical study. J Geophys Res Space Phys 103(A3):4327–4341

Knudsen DJ, Burchill JK, Buchert SC, Eriksson AI, Gill R, Wahlund J-E, Åhlen L, Smith M, Moffat B (2017) Thermal ion imagers and langmuir probes in the swarm electric field instruments. J Geophys Res Space Phys 122(2):2655–2673

Lee TE, Miller SD, Turk FJ, Schueler C, Julian R, Deyo S, Dills P, Wang S (2006) The npoess viirs day/night visible sensor. Bull Am Meteorol Soc 87(2):191–200

Liu J, Lyons LR, Archer WE, Gallardo-Lacourt B, Nishimura Y, Zou Y, Gabrielse C, Weygand JM (2018) Flow shears at the poleward boundary of omega bands observed during conjunctions of swarm and themis asi. Geophys Res Lett 45(3):1218–1227

Liu J, Lyons LR, Wang C-P, Hairston MR, Zhang Y, Zou Y (2020) Dawnside auroral polarization streams. J Geophys Res Space Phys 125(8):e2019JA027742

MacDonald EA, Donovan E, Nishimura Y, Case NA, Gillies DM, Gallardo-Lacourt B, Archer WE, Spanswick EL, Bourassa N, Connors M, Heavner M, Jackel B, Kosar B, Knudsen DJ, Ratzlaff C, Schofield I (2018) New science in plain sight: citizen scientists lead to the discovery of optical structure in the upper atmosphere. Sci Adv 4(3):eaaq0030

Martinis C, Griffin I, Gallardo-Lacourt B, Wroten J, Nishimura Y, Baumgardner J, Knudsen DJ (2022) Rainbow of the night: first direct observation of a sar arc evolving into steve. Geophys Res Lett 49(11):e2022GL098511

Mende SB, Harding BJ, Turner C (2019) Subauroral green steve arcs: evidence for low-energy excitation. Geophysical Res Lett 46(24):14256–14262

Miller SD, Straka W, Mills SP, Elvidge CD, Lee TF, Solbrig J, Walther A, Heidinger AK, Weiss SC (2013) Illuminating the capabilities of the suomi national polar-orbiting partnership (npp) visible infrared imaging radiometer suite (viirs) day/night band. Remote Sensing 5(12):6717–6766

Mishin E, Streltsov A (2022) On the kinetic theory of subauroral arcs. J Geophys Res Space Phys 127(8):e2022JA030667

Motoba T, Hosokawa K, Kadokura A, Sato N (2012) Magnetic conjugacy of northern and southern auroral beads. Geophys Res Lett 39(8)

Nanjo S, Nozawa S, Yamamoto M, Kawabata T, Johnsen MG, Tsuda TT, Hosokawa K (2022) An automated auroral detection system using deep learning: real-time operation in tromsø, norway. Sci Rep 12(1):8038

Nishimura Y, Donovan EF, Angelopoulos V, Nishitani N (2020) Dynamics of auroral precipitation boundaries associated with steve and said. J Geophys Res Space Phys 125(8):e2020JA028067

Nishimura Y, Dyer A, Donovan EF, Angelopoulos V (2023) Fine-scale structures of steve revealed by 4k imaging. J Geophys Res Space Phys 128(12):e2023JA032008

Nishimura Y, Dyer A, Kangas L, Donovan E, Angelopoulos V (2023) Unsolved problems in strong thermal emission velocity enhancement (steve) and the picket fence. Front Astron Space Sci 10:1087974

Ogawa Y, Kadokura A, Ejiri M (2020) Optical calibration system of nipr for aurora and airglow observations. Polar Sci 26:100570

Oyama S, Shinbori A, Ogawa Y, Kellinsalmi M, Raita T, Aikio A, Vanhamäki H, Shiokawa K, Virtanen I, Cai L, Workayehu AB, Pedersen M, Kauristie K, Tsuda TT, Kozelov B, Demekhov A, Yahnin A, Tsuchiya F, Kumamoto A, Kasahara Y, Matsuoka A, Shoji M, Teramoto M, Lester M (2020) An ephemeral red arc appeared at 68° mlat at a pseudo breakup during geomagnetically quiet conditions. J Geophys Res Space Phys 125(10):e2020JA028468

Semeter J, Hunnekuhl M, MacDonald E, Hirsch M, Zeller N, Chernenkoff A, Wang J (2020) The mysterious green streaks below steve. AGU Adv 1(4):e2020AV000183. https://doi.org/10.1029/2020AV000183

Shiokawa K, Katoh Y, Satoh M, Ejiri MK, Ogawa T, Nakamura T, Tsuda T, Wiens RH (1999) Development of optical mesosphere thermosphere imagers (omti). Earth Planets Space 51(7):887–896

Shiokawa K, Otsuka Y, Connors M (2019) Statistical study of auroral/resonant-scattering 427.8-nm emission observed at subauroral latitudes over 14 years. J Geophys Res Space Phys 124(11):9293–9301

Spiro RW, Heelis RA, Hanson WB (1979) Rapid subauroral ion drifts observed by atmosphere explorer c. Geophys Res Lett 6(8):657–660

Tanaka Y, Umemura N, Abe S, Shinbori A, UeNo S (2023) Advanced tools for guiding data-led research processes of upper-atmospheric phenomena. Geosci Data J 10(1):130–141

Yadav S, Shiokawa K, Otsuka Y, Connors M, St Maurice J-P (2021) Multi-wavelength imaging observations of steve at athabasca, canada. J Geophys Res Space Phys 126(2):2020JA028622

Zinke S (2017) A simplified high and near-constant contrast approach for the display of viirs day/night band imagery. Int J Remote Sensing 38(19):5374–5387

Zmuda AJ, Armstrong JC (1974) The diurnal flow pattern of field-aligned currents. J Geophys Res 79(31):4611–4619

Publisher's Note

Springer Nature remains neutral with regard to jurisdictional claims in published maps and institutional affiliations.